

## Strong tunable coupling between two distant superconducting spin qubits

Pita-Vidal, Marta; Wesdorp, Jaap J.; Splitthoff, Lukas J.; Bargerbos, Arno; Liu, Yu; Kouwenhoven, Leo P.; Andersen, Christian Kraglund

**DOI**

[10.1038/s41567-024-02497-x](https://doi.org/10.1038/s41567-024-02497-x)

**Publication date**

2024

**Document Version**

Final published version

**Published in**

Nature Physics

**Citation (APA)**

Pita-Vidal, M., Wesdorp, J. J., Splitthoff, L. J., Bargerbos, A., Liu, Y., Kouwenhoven, L. P., & Andersen, C. K. (2024). Strong tunable coupling between two distant superconducting spin qubits. *Nature Physics*, 20, 1158-1163. <https://doi.org/10.1038/s41567-024-02497-x>

**Important note**

To cite this publication, please use the final published version (if applicable).  
Please check the document version above.

**Copyright**

Other than for strictly personal use, it is not permitted to download, forward or distribute the text or part of it, without the consent of the author(s) and/or copyright holder(s), unless the work is under an open content license such as Creative Commons.

**Takedown policy**

Please contact us and provide details if you believe this document breaches copyrights.  
We will remove access to the work immediately and investigate your claim.

# Strong tunable coupling between two distant superconducting spin qubits

Received: 21 August 2023

Accepted: 28 March 2024

Published online: 06 May 2024

 Check for updates

Marta Pita-Vidal <sup>1,3</sup>✉, Jaap J. Wesdorp <sup>1,3</sup>, Lukas J. Splitthoff <sup>1</sup>,  
Arno Bargerbos<sup>1</sup>, Yu Liu <sup>2</sup>, Leo P. Kouwenhoven<sup>1</sup> &  
Christian Kraglund Andersen <sup>1</sup>✉

Andreev spin qubits have recently emerged as an alternative qubit platform with realizations in semiconductor–superconductor hybrid nanowires. In these qubits, the spin degree of freedom of a quasiparticle trapped in a Josephson junction is intrinsically spin–orbit coupled to the supercurrent across the junction. This interaction has previously been used to perform spin readout, but it has also been predicted to facilitate inductive multi-qubit coupling. Here we demonstrate a strong supercurrent-mediated longitudinal coupling between two distant Andreev spin qubits. We show that it is both gate- and flux-tunable into the strong coupling regime and, furthermore, that magnetic flux can be used to switch off the coupling in situ. Our results demonstrate that integrating microscopic spin states into a superconducting qubit architecture can combine the advantages of both semiconductors and superconducting circuits and pave the way to fast two-qubit gates between distant spins.

Semiconducting spin qubits<sup>1,2</sup> have proven to be a promising platform for quantum information processing. In such qubits, quantum information is encoded in the spin degree of freedom of electrons or holes localized in quantum dots, which leads to long lifetimes and a naturally large energy separation between computational and non-computational states. Moreover, their small size makes them attractive candidates for large-scale quantum devices<sup>3,4</sup>. However, it remains challenging to engineer a direct spin–spin coupling between remote spin qubits as their interaction strength decays rapidly with distance. Ongoing efforts to overcome this challenge focus on engineering a coupling between distant spin qubits mediated by microwave photons in superconducting resonators<sup>5–10</sup>. For such photon-mediated spin–spin coupling, the interaction strength is currently limited to the order of 10 MHz, which makes the implementation of fast, long-range two-qubit gates an outstanding challenge<sup>4,9</sup>. Moreover, the transverse character of the coupling puts a constraint on the available qubit frequencies.

An alternative approach to engineer remote spin–spin coupling is to embed the spin qubit into a Josephson junction, creating a so-called Andreev spin qubit (ASQ)<sup>11,12</sup>, where the qubit states carry

a spin-dependent supercurrent<sup>11–17</sup>. Recent experiments have demonstrated that a single ASQ can be operated coherently with strong coupling of the spin states to superconducting circuits<sup>11,12</sup>. Similarly, it has been predicted that large spin-dependent supercurrents can lead to strong, longitudinal, long-range and tunable spin–spin coupling<sup>18,19</sup>, thus overcoming the challenges imposed by the coupling being only a second-order interaction in previous photon-mediated implementations of spin–spin coupling as well as circumventing any strong constraints on the qubit frequencies.

Here, we investigate the supercurrent-mediated coupling between two ASQs by analysing the influence of a shared Josephson inductance on the coupling strength using the setup in Fig. 1. Specifically, we design a device formed by two ASQs, ASQ1 and ASQ2, connected in parallel to a third Josephson junction with gate-tunable Josephson inductance, thus defining two superconducting loops (Fig. 1a). Microscopically, the longitudinal coupling between the qubits directly results from the main characteristic of ASQs: their spin to supercurrent coupling. Part of the spin-state-dependent supercurrent of one qubit circulates through the loop arm containing the other qubit. This in turn causes

<sup>1</sup>QuTech and Kavli Institute of Nanoscience, Delft University of Technology, Delft, the Netherlands. <sup>2</sup>Center for Quantum Devices, Niels Bohr Institute, University of Copenhagen, Copenhagen, Denmark. <sup>3</sup>These authors contributed equally: Marta Pita-Vidal, Jaap J. Wesdorp. ✉e-mail: [m.pitavidal@tudelft.nl](mailto:m.pitavidal@tudelft.nl); [c.k.andersen@tudelft.nl](mailto:c.k.andersen@tudelft.nl)

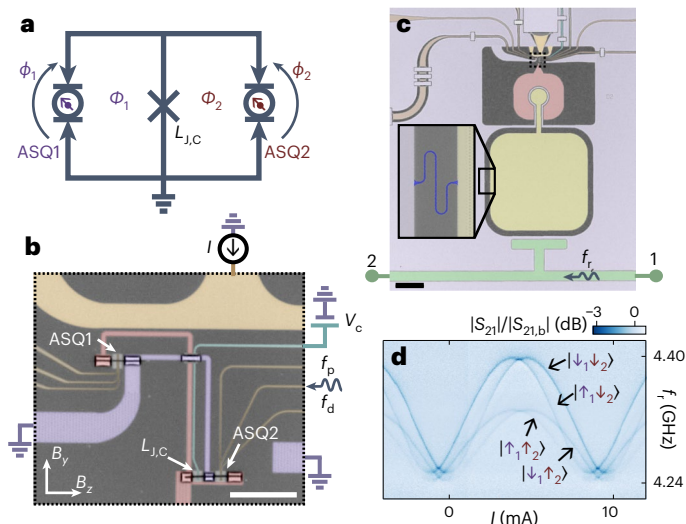


**Fig. 1 | Device and readout.** **a**, Circuit diagram of two coupled ASQs (ASQ1 and ASQ2) connected to a coupling junction with a tunable Josephson inductance  $L_{J,C}$ .  $\Phi_1$  and  $\Phi_2$  are the magnetic fluxes through the two loops. **b**, False-coloured optical microscope image of the device. The ASQs are placed between a transmon island (red) and ground (purple). The three Josephson junctions are implemented in two separate Al/InAs nanowires, with one containing ASQ1 and the other containing ASQ2 and the coupling junction. The in-plane magnetic field directions are denoted as  $B_z$  and  $B_y$ , approximately parallel and perpendicular to the nanowires axis, respectively. Additional flux control is achieved through the applied current  $I$  in the flux line (amber). Each ASQ is electrostatically controlled by three gates below the nanowire (brown), and the coupling junction is controlled by one gate line (cyan) at voltage  $V_C$ . The drive tones  $f_d$  and  $f_p$  are applied through the central gate of ASQ2. See Supplementary Fig. 5 for further details about the geometry of the loops area. **c**, Zoomed-out false-coloured optical microscope image showing the transmon island (red) capacitively coupled to a lumped-element readout resonator consisting of a capacitor (yellow) and an inductor (blue, inset). The resonator is further capacitively coupled to a coplanar waveguide (green centre conductor) with input and output ports labelled 1 and 2, respectively. A readout tone  $f_r$  is applied through the waveguide. **d**, Amplitude of the transmission through the readout circuit,  $|S_{21}|$ , divided by the background,  $|S_{21,b}|$ , as a function of the current through the flux line,  $I$ . The measurement is performed at a magnetic field of  $B_z = 0$  with a fixed  $\Phi_2 \approx -\Phi_0/4$ , set by  $B_y = -1.04$  mT. Scale bars, 10  $\mu\text{m}$  (**b**), 100  $\mu\text{m}$  (**c**).

a phase difference across the second qubit and hence affects its spin transition frequency. We show that the qubit–qubit coupling in this configuration can be in situ controlled by the flux through the superconducting loops as well as by changing the Josephson inductance of the shared junction using an electrostatic gate. In particular, we reach the strong longitudinal coupling regime where the coupling strength is larger than the qubit linewidths. Moreover, we show that the coupling can be switched fully off for particular values of the flux, which makes this platform appealing as an alternative for implementing fast flux-controlled two-qubit gates between spin qubits.

## Device

In our device, each ASQ is hosted in a quantum dot Josephson junction that is implemented in a separate Al/InAs nanowire and controlled by three electrostatic gates placed beneath the nanowires (Fig. 1b). Throughout this work, the gate voltages are fixed as specified in Supplementary Table 2 (see also Supplementary Information, which contains further details about the theoretical expression for the coupling strength, fabrication and experimental setup, device tuneup and additional data). Moreover, we define an additional regular Josephson junction with gate-tunable Josephson inductance  $L_{J,C}$  in one of the nanowires. The nanowires are galvanically connected to a NbTiN circuit that defines the superconducting loops forming a double-loop superconducting

quantum interference device (SQUID). We denote by  $\Phi_1$  and  $\Phi_2$  the external magnetic fluxes through each of the loops. The qubit frequency for ASQ $i$ ,  $f_i$ , where  $i = 1, 2$ , is set by the energy difference between the spin states,  $|\uparrow_i\rangle$  and  $|\downarrow_i\rangle$ , which is controlled by the magnetic field due to the Zeeman effect. We denote the in-plane magnetic field directions as  $B_z$ , approximately along the nanowires, and  $B_y$ , approximately perpendicular to the nanowires. See also Supplementary Section III.E for additional details on the field alignment. The  $B_y$  component of the magnetic field is moreover used to tune  $\Phi_1$  and  $\Phi_2$ . Note that although  $B_y$  is applied in the chip plane, it still threads flux through the loops due to the elevation of the nanowires with respect to the NbTiN circuitry. This reduces flux jumps compared to using out-of-plane field  $B_x$  for flux tuning, as discussed in ref. 16.  $\Phi_1$  and  $\Phi_2$  set the phase drops over the junctions,  $\phi_1 \approx \frac{2\pi}{\Phi_0} \Phi_1$  and  $\phi_2 \approx \frac{2\pi}{\Phi_0} \Phi_2$  in the limit of small  $L_{J,C}$ ,

where  $\Phi_0$  denotes the magnetic flux quantum. The current through the flux line,  $I$ , tunes  $\Phi_1$  and leaves  $\Phi_2$  nearly unaffected, as the loop corresponding to  $\Phi_2$  is placed near the symmetry axis of the flux line (Supplementary Fig. 4). The drive pulses, with frequencies  $f_d$  and  $f_p$ , are sent through the central gate of ASQ2 and are used to drive both qubits. We find that it is possible to drive ASQ1 using the gate line of ASQ2 possibly due to cross-coupling between the gate lines corresponding to both qubits or to cross-coupling between the gate line and the transmon island. The coupling junction is controlled by a single electrostatic gate whose voltage,  $V_C$ , is varied to tune  $L_{J,C}$ <sup>20</sup>.

To enable readout of the ASQ states, the double-loop SQUID in which the ASQs are hosted is placed between a superconducting island (red) and ground (purple), forming a transmon circuit<sup>21–23</sup> (Fig. 1b,c). These circuit elements are implemented in 20-nm-thick NbTiN for magnetic field compatibility<sup>16,24–29</sup>. The transmon frequency depends on the energy–phase relation of the double-loop SQUID, which in turn depends on the states of both ASQs<sup>17</sup>. The transmon is subsequently dispersively coupled to a lumped-element readout resonator, which is coupled to a feedline implemented with a coplanar waveguide and monitored in transmission using a probe tone at frequency  $f_r$ . The readout mechanism is illustrated in Fig. 1d, which shows the four possible frequencies of the readout resonator caused by the different dispersive shifts of the four spin states of the combined ASQ1–ASQ2 system<sup>30</sup>:  $\{|\uparrow_1\uparrow_2\rangle, |\uparrow_1\downarrow_2\rangle, |\downarrow_1\uparrow_2\rangle, |\downarrow_1\downarrow_2\rangle\}$ . Note that spin is not a well-defined quantum number for these states. In an ASQ, the spin is hybridized with spatial degrees of freedom, and thus the eigenstates are rather pseudospin states. Similar to previous works<sup>11,12</sup>, we will refer to the eigenstates as spins for simplicity. The measurement is taken at zero magnetic field where all spin states are thermally occupied on average, because the energy splitting between them is between 0.5 and 1 GHz (Supplementary Section III.C), which is smaller than typical effective temperatures on the order of 100 mK observed in these devices<sup>12</sup>. Therefore, the lines corresponding to all four states are visible. This result already illustrates the presence of two separate ASQs in the system. We will now move on to the characterization of these qubits before we turn our attention to the two-qubit coupling.

## Individual ASQ characterization

We first characterize each ASQ separately while the junction containing the other qubit is pinched off electrostatically using the voltages on its gates (Fig. 2), following the methods of ref. 12. To set the qubit frequencies, we apply a magnetic field  $B_z = 35$  mT in the  $y$ – $z$  plane, 0.1 radians from the  $B_z$  direction (Supplementary Section III.E). This field sets  $f_1 \in [6, 9]$  GHz and  $f_2 \in [2, 4.5]$  GHz for ASQ1 and ASQ2, respectively. We note that the qubit frequencies are different due to mesoscopic fluctuations in the gate dependence of the spin–orbit direction and  $g$ -factor of each ASQ (see also Fig. 2 and Supplementary Section III.C). Qubit spectroscopy is then performed by monitoring the transmission through the feedline near the readout-resonator frequency while applying a drive tone with frequency  $f_d$  to the central gate line of ASQ2

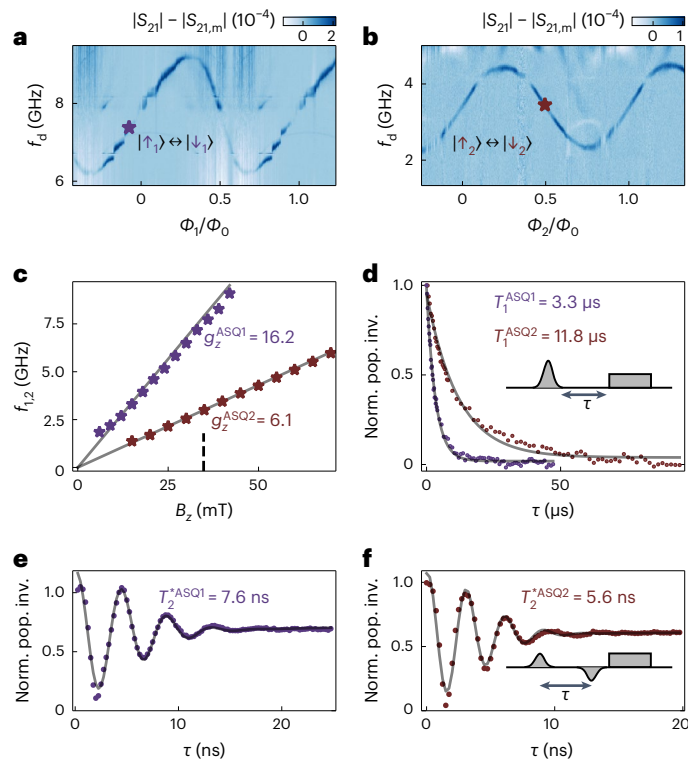


**Fig. 2 | Individual ASQ properties.** **a, b**, Readout signal amplitude with the median background subtracted,  $|S_{21}| - |S_{21,m}|$ , showing qubit spectroscopy of ASQ1 (versus  $\Phi_1$ ) (**a**) and ASQ2 (versus  $\Phi_2$ ) (**b**), respectively. During spectroscopy of one qubit, the other qubit is turned off by setting its gates to  $-1$  V. We set  $B_z = 35$  mT for both panels (indicated in **c** with a dashed line). **c**, Qubit frequency versus  $B_z$  for both ASQs.  $f_i$  is calculated as the average between its maximum and minimum values versus flux. The grey lines indicate a linear fit to the data from which we extract the  $g$ -factors indicated in the labels. **d**, Energy decay time ( $T_1$ ) measurements of both ASQs at the frequency setpoints indicated in **a** and **b** ( $f_1 = 7.4$  GHz and  $f_2 = 3.4$  GHz, respectively). The experiment was performed by sending a  $\pi$ -pulse followed, after a delay  $\tau$ , by a readout pulse (inset). **e, f**, Measurements of the coherence times ( $T_2^*$ ) of ASQ1 and ASQ2 at the same setpoints, measured using a Ramsey experiment. Oscillations with a period of 4 ns (**e**) and 3 ns (**f**) are realized by adding a phase to the final  $\pi/2$ -pulse proportional to the delay time  $\tau$ . The pulse sequence is shown in the inset for a phase of  $\pi$ .  $T_2^*$  is extracted by fitting a sine with a Gaussian decay envelope. The experiments were performed using Gaussian pulses with a full width at half-maximum of 4 ns. All datasets are averaged over  $3 \times 10^5$  shots, readout time ranges from 1 to 2  $\mu$ s, and the total measurement time for  $T_2^{*,ASQ_i}$  ranges from around 10 min for ASQ1 to around 30 min for ASQ2. The normalized population inversion (norm. pop. inv.) on the y axis of panels **d–f** is defined as the measured signal normalized by the signal difference between having sent no pulse and a  $\pi$ -pulse before the readout pulse.

(Fig. 2a,b). On resonance with the qubit transition, we observe a strong change in transmission because spin–orbit coupling and a magnetic field enable electrical driving of the spin<sup>16,17,31</sup>. The qubit frequencies,  $f_1$  and  $f_2$ , can be tuned by flux, as shown in Fig. 2a,b. Note that the phase dispersion is expected to be sinusoidal (refs. 19,32), as is the case for ASQ2. However, for ASQ1 we rather observe a skewed sine. From the ratio of the inductance of ASQ1 and  $L_{J,C}$  we rule out a non-linear flux-phase relation. This could indicate that non-zero-length effects beyond the model from refs. 17<sup>19</sup> in combination with higher orbitals in the quantum dot must be considered to accurately describe the physics of the junction containing ASQ1. Although flux tuning provides fine-tuning of the qubit frequency within a frequency band of a few GHz set by the spin–orbit coupling strength, we can also tune the qubit frequencies over a larger range by varying the magnetic field, due to the Zeeman effect. From the magnetic field dependence of the frequencies, we extract the  $g$ -factor

of each ASQ (Fig. 2c). We find that the different  $g$ -factors are consistent with earlier work<sup>16,17,33</sup> (see also Supplementary Section III.E).

Next, we characterize the coherence properties of each ASQ at the frequencies indicated with markers in Fig. 2a,b. At these setpoints, we extract energy decay times of  $T_1^{ASQ1} = 3.3 \pm 0.1 \mu$ s and  $T_1^{ASQ2} = 11.8 \pm 0.4 \mu$ s for ASQ1 and ASQ2, respectively, where the reported uncertainties are the  $1\sigma$  confidence intervals from the fit. These decay times are to a large extent limited by Purcell decay to the transmon qubit (Supplementary Section IV.B). Furthermore, from a Ramsey experiment, we extract dephasing times of  $T_2^{*ASQ1} = 7.6 \pm 0.2$  ns and  $T_2^{*ASQ2} = 5.6 \pm 0.2$  ns for ASQ1 and ASQ2, respectively, which are comparable to times found in earlier works<sup>11,12</sup>. For these measurements, we use Gaussian pulses with a full width at half-maximum of 4 ns, which is comparable to  $T_2^*$ . Therefore, the  $\pi/2$ -pulses cannot be considered instantaneous, which is the conventional assumption in a Ramsey experiment. Rather, a non-zero overlap of the pulses of order  $T_2^*$  can result in an overestimation of the extracted  $T_2^*$ , as further discussed in Supplementary Section IV.C. Therefore, these numbers should be interpreted as an upper bound to the pure dephasing times. Furthermore, we extract echo times of  $T_{2E}^{ASQ1} = 17.3 \pm 0.4$  ns and  $T_{2E}^{ASQ2} = 17.4 \pm 0.4$  ns (Supplementary Section IV.A, three times larger than  $T_2^*$ , which points at low-frequency noise being a strong contributor to dephasing, consistent with previous observations in InAs-based spin qubits<sup>11,12,34</sup>).

## Longitudinal coupling

Having two ASQs, we describe the joint system by the following Hamiltonian with the two qubits coupled longitudinally with coupling strength<sup>19</sup>:

$$H = -\frac{\hbar\omega_1}{2}\sigma_1^z - \frac{\hbar\omega_2}{2}\sigma_2^z - \frac{\hbar J}{2}\sigma_1^z\sigma_2^z, \quad (1)$$

where  $\omega_i = 2\pi f_i$  and  $\sigma_i^z = |\downarrow_i\rangle\langle\downarrow_i| - |\uparrow_i\rangle\langle\uparrow_i|$  denote the phase-dependent spin-flip frequency and the  $z$  Pauli matrix of ASQ $i$ , respectively,  $\hbar$  is the Planck constant and  $\hbar = h/(2\pi)$ . In this description, the longitudinal term  $-\frac{\hbar J}{2}\sigma_1^z\sigma_2^z$  originates from the fact that the spin-dependent supercurrent of ASQ1 induces a spin-dependent phase difference over ASQ2, thus changing its transition frequency by  $\pm J$  and vice versa. Importantly, the longitudinal coupling does not arise from direct wavefunction overlap<sup>35</sup> or magnetic interactions as the spins are separated by a distance of approximately 25  $\mu$ m. From this physical understanding of the interaction, we can express the coupling strength  $J$  as a function of the circuit parameters by<sup>19</sup>

$$J(L_{J,C}, \Phi_1, \Phi_2) = \frac{1}{2\hbar} \frac{L_{J,C} L_{ASQ}(\Phi_1, \Phi_2)}{L_{J,C} + L_{ASQ}(\Phi_1, \Phi_2)} I_1(\Phi_1) I_2(\Phi_2). \quad (2)$$

Here, we define  $L_{ASQ}(\Phi_1, \Phi_2)$  as the total spin-independent inductance of the two ASQs in parallel.  $I_i(\Phi_i)$  denotes twice the spin-dependent supercurrent through ASQ $i$ , which we define as the difference in supercurrent across ASQ $i$  for its two possible spin states. In this expression, one of the main features of the device becomes apparent: the coupling is tunable with flux and can be switched to zero when either  $I_1$  or  $I_2$  is set to zero.

We now proceed to investigate the spin–spin coupling at the same gate voltages and magnetic field used for Fig. 2. To this end, we open both loops simultaneously and set  $\Phi_1$  and  $\Phi_2$  at points where the slopes of the qubit frequencies  $\partial f_i/\partial \Phi_i \propto I_i$  are large, close to  $\Phi_1 \approx 0$  and  $\Phi_2 \approx \Phi_0/2$ . When the two qubits are longitudinally coupled, the transition frequency of each of them depends on the state of the other, as schematically depicted in Fig. 3a,d. In each panel, the blue arrows indicate the two possible frequencies of one qubit, separated by twice

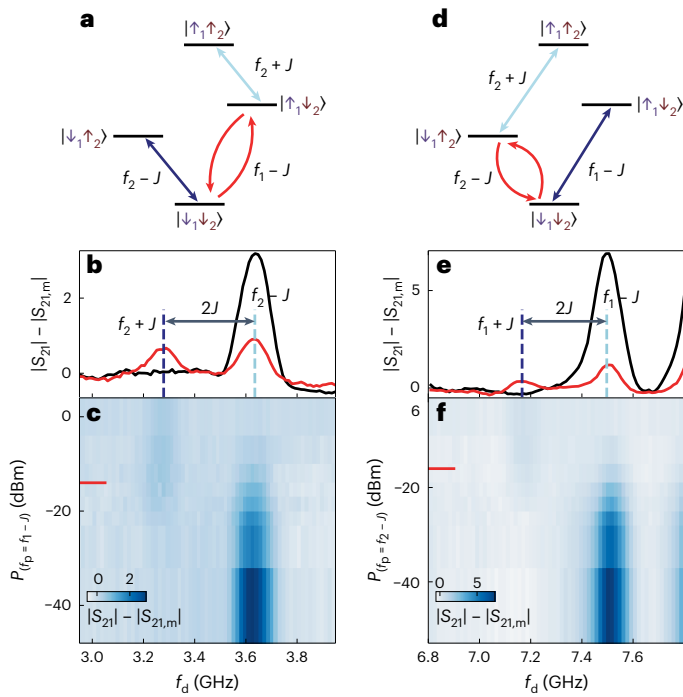


**Fig. 3 | Strong longitudinal coupling between the two ASQs.** **a**, Energy-level diagram of the combined ASQ1–ASQ2 system with the levels (horizontal black lines) labelled by the states of both qubits (ASQ1 in purple, ASQ2 in maroon). The diagonal arrows denote the two different transition frequencies ( $f_2 \pm J$ ) of ASQ2 depending on the state of ASQ1. Note that  $J$  is negative in this illustration and for the data presented in this figure. **b**, Spectroscopy of ASQ2 as a function of the drive frequency  $f_d$ . The black and red lines indicate the readout signal amplitude with the background subtracted,  $|S_{21}| - |S_{21,m}|$ , with and without a pump tone resonant with ASQ1 at frequency  $f_p = f_1 - J$ , respectively. The pump tone is indicated with red arrows in **a**. **c**, Power dependence of the pump tone. The red line indicates the power used for the red line in **b**. We indicate the power at the source output. **d–f**, Analogous to panels **a**, **b** and **c**, respectively, but with the roles of ASQ1 and ASQ2 exchanged. In this case, the pump tone drives ASQ2 at a frequency  $f_p = f_2 - J$  while performing spectroscopy of ASQ1.

the coupling strength,  $J$ , for the two possible states of the other qubit. To determine the magnitude of the coupling strength, we perform the following measurements: first we determine  $f_2 - J$  by performing qubit spectroscopy of ASQ2 starting from the ground state,  $|\downarrow_1\downarrow_2\rangle$ , where ASQ1 is in the spin-down state (black trace in Fig. 3b). Then we repeat the spectroscopy while applying another continuous pump tone at a frequency  $f_p$  resonant with the spin-flip transition of ASQ1, driving  $|\downarrow_1\downarrow_2\rangle \leftrightarrow |\uparrow_1\downarrow_2\rangle$ . The presence of this additional tone results in ASQ1 being in a mixture of  $|\downarrow_1\rangle$  and  $|\uparrow_1\rangle$ . When performing spectroscopy of ASQ2 under these conditions (red trace in Fig. 3b), we observe the emergence of a second peak corresponding to the shifted frequency of ASQ2 due to ASQ1 having population in its excited state,  $|\uparrow_1\rangle$ . This frequency splitting arises from the longitudinal coupling term, and thus we determine the value of  $J = -178 \pm 3$  MHz from a double Gaussian fit as half of the difference between the two frequencies (see Supplementary Section II.E.2 for details on the fit procedure). Since the coupling term is symmetric with respect to the two qubits, we should observe the same frequency splitting when we exchange the roles of ASQ1 and ASQ2 (Fig. 3e). (Note that the increase in amplitude around 7.8 GHz is unrelated to the ASQs but due to a resonance of the travelling wave parametric amplifier.) From this measurement, we extract a value of  $J = -165 \pm 4$  MHz, similar to the value we extracted before. We speculate that the modest difference between the values of  $J$  extracted from the measurements of both qubits may be due to temporal instabilities, which we found to be present in the system.

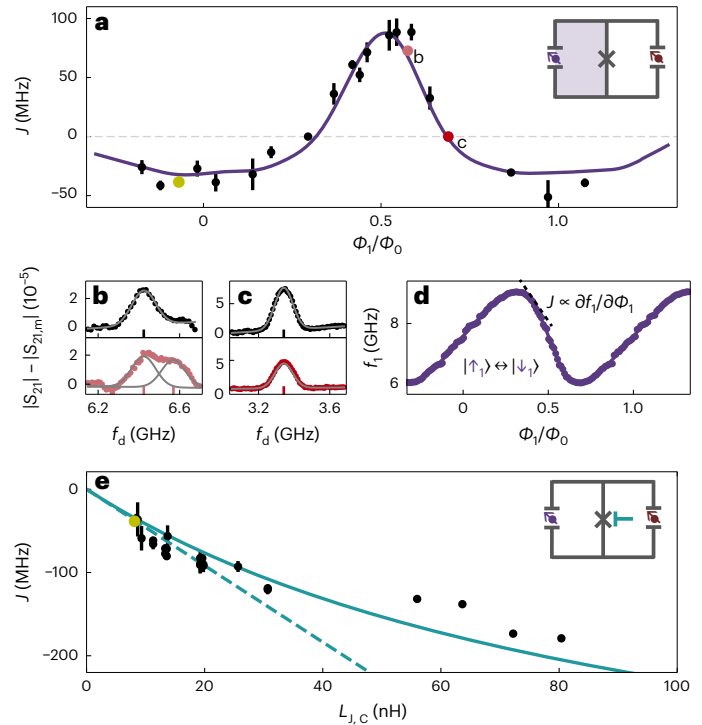


**Fig. 4 | Tunability of the coupling strength.** **a**, Qubit–qubit coupling strength,  $J$ , as a function of flux in the loop containing ASQ1,  $\Phi_1$ , (see also inset) at fixed  $\Phi_2 \approx 0.51\Phi_0$ . The purple line shows the expected dependence from equation (2). **b, c**, Representative fits at two  $\Phi_1$  points highlighted with coloured (and letter-marked) markers in **a**. The signal measured in the absence of a pump tone (black markers) is fit with a single Gaussian (black line) to determine  $f_1 - J$  (vertical black line in the  $x$  axis). The signal measured in the presence of a pump tone at the other ASQ (pink and red markers in **b** and **c**, respectively) is additionally fitted (pink and red line in **b** and **c**, respectively) to determine  $f_1 + J$ . The grey lines in **b** show the two individual Gaussians. **d**, Frequency of ASQ1,  $f_1$ , versus  $\Phi_1$  (markers) and interpolation (line) used to estimate  $I_1(\Phi_1) \approx \hbar \partial f_1 / \partial \Phi_1$ . **e**, Qubit–qubit coupling strength  $J$  at fixed  $\Phi_1 = -0.07\Phi_0$  and as a function of  $L_{J,c}$ , which is varied using the gate voltage at the coupling junction (inset). The continuous line shows the dependence from equation (2), and the dashed line shows a linear dependence  $Jh = L_{J,c}I_1I_2/2$ . The yellow marker in **a** and **e** is a shared point between the two panels. In **a** and **e**, the markers and error bars represent the best-fit values of  $J$  (**b, c**) and their estimated standard errors ( $1\sigma$  confidence intervals), respectively.

We additionally measure the qubit spectroscopy as a function of the pump tone power, shown in Fig. 3c, f, and we observe a power dependence on the peak amplitude. At low powers, not enough excited population is generated in the ASQ, whereas the second peak gradually appears at higher powers. At too-high powers, the readout resonator shifts too much due to the non-linearity of the resonator mode, and it becomes more lossy, which results in a reduced signal (at even higher power, both peaks fully disappear). Additional data and a numerical analysis of the expected pump power dependence and relative peak heights, in agreement with the experimental observations, can be found in Supplementary Sections V and I.D, respectively.

Next, we compare the extracted value of  $J$  to the linewidth of the ASQ transitions and find  $J = 165$  MHz  $> 28$  MHz  $= 1/(2\pi T_2^{*ASQ2})$ , indicating that the system is in the strong longitudinal coupling regime. This value of  $J$  puts a speed limit on a controlled-Z two-qubit gate at a time of  $t = 1/(4J) = 1.4$  ns and a coherence limit on the average gate fidelity of around 85%, which will be explored in future experiments. Such a two-qubit gate, combined with single-qubit rotations, enables a universal set of gates. On the other hand, such a fast gate would require distortion-free flux pulses<sup>36</sup>, with a rise time much smaller

than the gate time of 1.5 ns. This two-qubit gate time is much faster than typical fast two-qubit gates with superconducting qubits (10–45 ns (refs. 37,38)) and comparable to the fastest short-distance exchange gates in spin qubits coupled via directly overlapping wavefunctions<sup>1,39,40</sup>.

## Tunability of the coupling strength

We have so far investigated the coupling strength at fixed gate voltages and flux. We now investigate the dependence of  $J$  on different control parameters and demonstrate that it is tunable as predicted by equation (2) (ref. 19). We vary  $\Phi_1$  using the flux line (Fig. 4a) and find that the coupling strength is directly proportional to  $I_1$ , as expected. The current difference across ASQ1,  $I_1$ , is extracted from a measurement of the qubit frequency as a function of flux, as shown in Fig. 4d. Note that by varying the flux, we not only vary the magnitude of  $J$  but also switch its sign, crossing zero coupling. Thus the two ASQs can be fully uncoupled by setting  $J = 0$  at the flux points that maximize or minimize  $f_1(\Phi_1)$  and where thus  $I_1 = 0$ , for either of the qubits. The coinciding of zero coupling with these frequency extrema is useful as these are the first-order flux-insensitive points of the qubit transition frequency. Two representative situations in which the ASQs are coupled and uncoupled at nearby flux points are shown in Fig. 4b,c, respectively. The data were measured and analysed using the same procedure described for Fig. 3.

We overlay the  $\Phi_1$  dependence of the coupling strength with the expected dependence from equation (2). The values of  $L_{J,C} = 8.4$  nH and  $I_2 \approx \hbar \partial f_2 / \partial \Phi_2 |_{\Phi_2 = 0.51 \Phi_0} = -2.52$  nA are fixed and independently extracted from measurements of the transmon frequency and of  $f_2(\Phi_2)$ , respectively.  $L_{ASQ}(\Phi_1)$  is calculated as the parallel combination of the spin-independent Josephson inductances of both qubits, which are determined from separate transmon spectroscopy measurements (Supplementary Section III.C), and  $I_1(\Phi_1) \approx \hbar \partial f_1 / \partial \Phi_1$  is estimated from Fig. 4d. As shown in Fig. 4a, the measured  $J(\Phi_1)$  is in good agreement with equation (2).

Finally, we investigate the  $L_{J,C}$  tunability of  $J$  by fixing  $\Phi_1 = -0.07 \Phi_0$ , which sets  $I_1 = 2.16$  nA, and varying the value of  $V_C$  (see Supplementary Section III.B for the corresponding qubit parameters). We observe an increase of the magnitude of  $J$  as the value of  $L_{J,C}$  is increased, as shown in Fig. 4e. The measured data follow to a large extent the dependence expected from equation (2), indicated with a continuous line in Fig. 4e. The  $|J|$  increase is limited to a maximum when the coupling junction  $L_{J,C}$  becomes comparable to the finite spin-independent inductance  $L_{ASQ}$  of the ASQs. For the solid line in Fig. 4e, we use the independently measured value  $L_{ASQ}(\Phi_1 = -0.07 \Phi_0, \Phi_2 = 0.51 \Phi_0) = 102.0$  nH. For comparison, the dashed line depicts the limit of  $L_{ASQ} \gg L_{J,C}$ .

## Conclusions

In conclusion, we have extended earlier results demonstrating single ASQs<sup>11,12</sup> and integrated two InAs/Al-based ASQs within a single transmon circuit. The two ASQs are separated by around 25  $\mu\text{m}$ , two orders of magnitude larger than the size of the individual qubit wavefunctions. Both ASQs showed coherence properties comparable to those reported in prior work<sup>11,12</sup>. We have shown strong supercurrent-mediated coupling between the two ASQs and found that the coupling strength,  $J$ , can be tuned with either a magnetic flux or an electrical voltage. In particular, we have shown that  $J$  can be fully suppressed using a magnetic flux. This switchability of the coupling is essential for the use of longitudinally coupled ASQs to perform quantum computation. Furthermore, the high sign and magnitude tunability of  $J$  could have applications for the use of ASQs to perform analogue quantum simulations. More generally, ASQs could in the future provide an independent platform for quantum computing and simulation or, alternatively, be incorporated into existing spin-qubit platforms and serve as read-out modules or long-distance couplers. Independently of the precise use case for ASQs, we emphasize that strong spin–spin coupling as

demonstrated here will be an essential requirement, although smaller dephasing rates would be desired.

Previous works suggest that one possible mechanism limiting dephasing is coupling to the large nuclear spins of InAs<sup>11,12,34</sup>. Although the origin of dephasing must be further investigated, this suggests that a possible route to increase the dephasing times is implementing ASQs in an alternative nuclear-spin-free material such as germanium<sup>41–45</sup>. We expect that future efforts using alternative materials could provide a path towards integration in more established semiconductor-based quantum architectures as well as strongly increased coherence times. If longer coherence times can be achieved in combination with the strong qubit–qubit coupling demonstrated here, ASQs will emerge as an encouraging platform for the realization of high-fidelity two-qubit gates between remote spins.

## Online content

Any methods, additional references, Nature Portfolio reporting summaries, source data, extended data, supplementary information, acknowledgements, peer review information; details of author contributions and competing interests; and statements of data and code availability are available at <https://doi.org/10.1038/s41567-024-02497-x>.

## References

- Loss, D. & DiVincenzo, D. P. Quantum computation with quantum dots. *Phys. Rev.* **120**–126 (1998).
- Hanson, R., Kouwenhoven, L. P., Petta, J. R., Tarucha, S. & Vandersypen, L. M. K. Spins in few-electron quantum dots. *Rev. Mod. Phys.* 127–1265 (2007).
- Vandersypen, L. M. K. et al. Interfacing spin qubits in quantum dots and donors—hot, dense, and coherent. *npj Quantum Inf.* **3**, 34 (2017).
- Burkard, G., Ladd, T. D., Pan, A., Nichol, J. M. & Petta, J. R. Semiconductor spin qubits. *Rev. Mod. Phys.* **95**, 025003 (2023).
- Mi, X. et al. A coherent spin–photon interface in silicon. *Nature* <https://doi.org/10.1038/nature25769> (2018).
- Samkharadze, N. et al. Strong spin–photon coupling in silicon. *Science* <https://doi.org/10.1126/science.aar4054> (2018).
- Landig, A. J. et al. Coherent spin–photon coupling using a resonant exchange qubit. *Nature* <https://doi.org/10.1038/s41586-018-0365-y> (2018).
- Borjans, F., Croot, X. G., Mi, X., Gullans, M. J. & Petta, J. R. Resonant microwave-mediated interactions between distant electron spins. *Nature* <https://doi.org/10.1038/s41586-019-1867-y> (2020).
- Harvey-Collard, P. et al. Coherent spin–spin coupling mediated by virtual microwave photons. *Phys. Rev. X* <https://doi.org/10.1103/physrevx.12.021026> (2022).
- Yu, C. X. et al. Strong coupling between a photon and a hole spin in silicon. *Nat. Nanotechnol.* <https://doi.org/10.1038/s41565-023-01332-3> (2023).
- Hays, M. et al. Coherent manipulation of an Andreev spin qubit. *Science* **373**, 430–433 (2021).
- Pita-Vidal, M. et al. Direct manipulation of a superconducting spin qubit strongly coupled to a transmon qubit. *Nat. Phys.* <https://doi.org/10.1038/s41567-023-02071-x> (2023).
- Tosi, L. et al. Spin-orbit splitting of Andreev states revealed by microwave spectroscopy. *Phys. Rev. X* <https://doi.org/10.1103/physrevx.9.011010> (2019).
- Hays, M. et al. Continuous monitoring of a trapped superconducting spin. *Nat. Phys.* <https://doi.org/10.1038/s41567-020-0952-3> (2020).
- Wesdorp, J. J. et al. Dynamical polarization of the fermion parity in a nanowire Josephson junction. *Phys. Rev. Lett.* **131**, 117001 (2023).
- Wesdorp, J. J. et al. Microwave spectroscopy of interacting Andreev spins. *Phys. Rev. B* **109**, 045302 (2024).

17. Bargerbos, A. et al. Spectroscopy of spin-split andreev levels in a quantum dot with superconducting leads. *Phys. Rev. Lett.* **131**, 097001 (2023).
18. Chtchelkatchev, N. M. & Nazarov, Y. V. Andreev quantum dots for spin manipulation. *Phys. Rev. Lett.* <https://doi.org/10.1103/PhysRevLett.90.226806> (2003).
19. Padurariu, C. & Nazarov, Y. V. Theoretical proposal for superconducting spin qubits. *Phys. Rev. B* <https://doi.org/10.1103/PhysRevB.81.144519> (2010).
20. Doh, Y.-J. et al. Tunable supercurrent through semiconductor nanowires. *Science* **309**, 272–275 (2005).
21. Koch, J. et al. Charge-insensitive qubit design derived from the cooper pair box. *Phys. Rev. A* <https://doi.org/10.1103/physreva.76.042319> (2007).
22. Larsen, T. W. et al. Semiconductor-nanowire-based superconducting qubit. *Phys. Rev. Lett.* <https://doi.org/10.1103/PhysRevLett.115.127001> (2015).
23. de Lange, G. et al. Realization of microwave quantum circuits using hybrid superconducting-semiconducting nanowire Josephson elements. *Phys. Rev. Lett.* <https://doi.org/10.1103/PhysRevLett.115.127002> (2015).
24. Samkharadze, N. et al. High-kinetic-inductance superconducting nanowire resonators for circuit QED in a magnetic field. *Phys. Rev. Appl.* <https://doi.org/10.1103/PhysRevApplied.5.044004> (2016).
25. Kroll, J. G. et al. Magnetic field compatible circuit quantum electrodynamics with graphene Josephson junctions. *Nat. Commun.* **9**, 4615 (2018).
26. Kroll, J. G. et al. Magnetic-field-resilient superconducting coplanar-waveguide resonators for hybrid circuit quantum electrodynamics experiments. *Phys. Rev. Appl.* <https://doi.org/10.1103/PhysRevApplied.11.064053> (2019).
27. Pita-Vidal, M. et al. Gate-tunable field-compatible fluxonium. *Phys. Rev. Appl.* <https://doi.org/10.1103/PhysRevApplied.14.064038> (2020).
28. Kringhøj, A. et al. Magnetic-field-compatible superconducting transmon qubit. *Phys. Rev. Appl.* **15**, 054001 (2021).
29. Uilhoorn, W. et al. Quasiparticle trapping by orbital effect in a hybrid superconducting-semiconducting circuit. Preprint at <https://arxiv.org/abs/2105.11038> (2021).
30. Blais, A., Huang, R.-S., Wallraff, A., Girvin, S. M. & Schoelkopf, R. J. Cavity quantum electrodynamics for superconducting electrical circuits: an architecture for quantum computation. *Phys. Rev. A* <https://doi.org/10.1103/PhysRevA.69.062320> (2004).
31. Metzger, C. et al. Circuit-QED with phase-biased Josephson weak links. *Phys. Rev. Res.* <https://doi.org/10.1103/physrevresearch.3.013036> (2021).
32. Pavešić, L., Vidal, M. P., Bargerbos, A. & Žitko, R. Impurity Knight shift in quantum dot Josephson junctions. *SciPost Phys.* **15**, 070 (2023).
33. Vaitiekėnas, S., Deng, M.-T., Nygård, J., Krogstrup, P. & Marcus, C. M. Effective  $g$  factor of subgap states in hybrid nanowires. *Phys. Rev. Lett.* **121**, 037703 (2018).
34. Nadj-Perge, S., Frolov, S. M., Bakkers, E. P. A. M. & Kouwenhoven, L. P. Spin-orbit qubit in a semiconductor nanowire. *Nature* <https://doi.org/10.1038/nature09682> (2010).
35. Spethmann, M., Zhang, X.-P., Klinovaja, J. & Loss, D. Coupled superconducting spin qubits with spin-orbit interaction. *Phys. Rev. B* **106**, 115411 (2022).
36. Rol, M. A. et al. Time-domain characterization and correction of on-chip distortion of control pulses in a quantum processor. *Appl. Phys. Lett.* **116**, 054001 (2020).
37. Arute, F. et al. Quantum supremacy using a programmable superconducting processor. *Nature* <https://doi.org/10.1038/s41586-019-1666-5> (2019).
38. Rol, M. A. et al. Fast, high-fidelity conditional-phase gate exploiting leakage interference in weakly anharmonic superconducting qubits. *Phys. Rev. Lett.* **123**, 120502 (2019).
39. He, Y. et al. A two-qubit gate between phosphorus donor electrons in silicon. *Nature* **571**, 371–375 (2019).
40. Hendrickx, N. W. et al. A four-qubit germanium quantum processor. *Nature* **591**, 580–585 (2021).
41. Hendrickx, N. W. et al. Gate-controlled quantum dots and superconductivity in planar germanium. *Nat. Commun.* <https://doi.org/10.1038/s41467-018-05299-x> (2018).
42. Vigneau, F. et al. Germanium quantum-well Josephson field-effect transistors and interferometers. *Nano Lett.* **19**, 1023–1027 (2019).
43. Scappucci, G. et al. The germanium quantum information route. *Nat. Rev. Mater.* <https://doi.org/10.1038/s41578-020-00262-z> (2021).
44. Tosato, A. et al. Hard superconducting gap in germanium. *Commun. Mater.* **4**, 23 (2023).
45. Valentini, M. et al. Radio frequency driven superconducting diode and parity conserving Cooper pair transport in a two-dimensional germanium hole gas. *Nat. Commun.* **15**, 169 (2024).

**Publisher's note** Springer Nature remains neutral with regard to jurisdictional claims in published maps and institutional affiliations.

Springer Nature or its licensor (e.g. a society or other partner) holds exclusive rights to this article under a publishing agreement with the author(s) or other rightsholder(s); author self-archiving of the accepted manuscript version of this article is solely governed by the terms of such publishing agreement and applicable law.

© The Author(s), under exclusive licence to Springer Nature Limited 2024

## Data availability

The data that support the findings of this study are publicly available via 4TU.ResearchData at <https://doi.org/10.4121/e10185d0-026e-480f-bbaa-3448c6e1b9a2>. Source data are provided with this paper.

## Code availability

The analysis code that supports the findings of this study is publicly available via 4TU.ResearchData at <https://doi.org/10.4121/e10185d0-026e-480f-bbaa-3448c6e1b9a2>.

## Acknowledgements

We thank B. van Heck, A. Kou, G. de Lange, V. Fatemi, P. Kurilovich, S. Diamond, T. Connolly, H. Nho, C. Boettcher, V. Kurilovich and X. Xue for discussions and their feedback on this paper. We thank Y. Nazarov for insightful discussions. We thank P. Krogstrup for guidance in the material growth. This work is part of the research project 'Scalable circuits of Majorana qubits with topological protection' (i39, SCMQ), project number 14SCMQ02, which is (partly) financed by the Dutch Research Council. It has further been supported by the Microsoft Quantum initiative. C.K.A. acknowledges support from the Dutch Research Council.

## Author contributions

J.J.W., M.P.-V. and C.K.A. conceived the experiment. Y.L. developed and provided the nanowire materials. J.J.W, M.P.-V., L.J.S. and A.B. prepared

the experimental setup and data acquisition tools. L.J.S. deposited the nanowires. J.J.W, M.P.-V. and A.B designed the device. J.J.W and M.P.-V. fabricated the device, performed the measurements and analysed the data, with continuous feedback from L.J.S., A.B. and C.K.A. L.P.K. and C.K.A. supervised the work. J.J.W., M.P.-V. and C.K.A. wrote the paper with feedback from all authors.

## Competing interests

The authors declare no competing interests.

## Additional information

**Supplementary information** The online version contains supplementary material available at <https://doi.org/10.1038/s41567-024-02497-x>.

**Correspondence and requests for materials** should be addressed to Marta Pita-Vidal or Christian Kraglund Andersen.

**Peer review information** *Nature Physics* thanks Jean-Damien Pillet and the other, anonymous, reviewer(s) for their contribution to the peer review of this work.

**Reprints and permissions information** is available at [www.nature.com/reprints](http://www.nature.com/reprints).